

Self-supervised Learning Framework for Remote Heart Rate Estimation Using Spatiotemporal Augmentation

Hao Wang, Euijoon Ahn, Jinman Kim

The University of Sydney
Sydney, NSW, Australia

hwang885@uni.sydney.edu.au, {euijoon.ahn, jinman.kim}@sydney.edu.au

Abstract

Recent supervised deep learning methods have shown that heart rate (HR) can be measured remotely using facial videos. However, the performance of these supervised methods are dependent on the availability of large-scale labelled data and they have been limited to 2D deep learning architectures that do not fully exploit the 3D spatiotemporal information. To solve this problem, We present a novel 3D self-supervised spatiotemporal learning framework for remote HR estimation on facial videos. Concretely, we propose a landmark-based spatial augmentation which splits the face into several informative parts based on the Shafer's dichromatic reflection model, and a novel sparsity-based temporal augmentation exploiting Nyquist–Shannon sampling theorem to enhance the signal modelling ability. We evaluated our method on 3 public datasets and outperformed other self-supervised methods and achieved competitive accuracy with the state-of-art supervised methods.

1. Introduction

Heart rate (HR) is a critical cardiovascular sign indicating the wellness of patients. Traditionally, the Electrocardiography (ECG) and Photoplethysmograph (PPG) are widely used to measure HR, and both of them rely on the availability of the cuff-based equipment which requires direct contact to human skin. This constrains the application of monitoring and estimating HR in an unobtrusive and concomitant way with ubiquitous devices (e.g., smartphone cameras, webcams) [29]. In recent years, non-contact video-based physiological measurement has been of great interest. Remote photoplethysmography (rPPG), using facial videos has been introduced to overcome the limitation of conventional contact-based measurement approaches. In rPPG, pulse signals are measured based on colour fluctuations on human skin, which are caused by the variations of blood volume during cardiac cycle [9].

Several recent studies using supervised deep learning methods [55, 54, 56, 41, 45, 32, 34, 33, 35, 24, 26, 6] have shown promising results to estimate HR. They, however, remain problematic because of their reliance on large amounts of labelled training data. Researchers have employed various approaches to help solve these challenges including deep learning with transferable knowledge across different domains and fine-tuning those knowledge with a relatively smaller amount of labelled image data. For example, Niu et al. [32] used the model that was pre-trained using large labelled natural images (i.e., ImageNet) and fine-tuned them using facial videos. An alternative approach is to use self-supervised learning to learn and extract image features from unlabelled data. Many recent self-supervised learning methods commonly apply the concept of contrastive learning and have achieved state-of-the-art performances in image/video representation learning [1, 37, 12, 40, 53, 14]. In these approaches, videos are transformed using standard data augmentation techniques such as image frame cropping, resizing, colour jittering and frame re-ordering to produce different views. Invariant video features are then learnt by maximising mutual information between those views in contrastive manner. These standard augmentation techniques, however, are mainly limited to learn features for action recognition tasks and they are not designed to capture the colour fluctuations on human skin. Many of HR estimation approaches also transformed the video frames (3D) into 2D spatiotemporal map for subsequent 2D convolutional neural networks (CNNs) training [34, 35, 41, 24]. However, this transformation potentially neglect nature information contained in original inputs [54].

In this paper, we present a new 3D Self-supervised Learning Framework for Heart Rate estimation (SLF-HR), where we design a landmark-based spatial augmentation using Shafer's dichromatic reflection model [50] to effectively capture the colour fluctuations on human face. We also propose a sparsity-based temporal augmentation that characterise periodic colour variations using Nyquist–Shannon sampling theorem [36]. We evaluated our method by

comparing with other state-of-the-art supervised and self-supervised approaches using 3 public datasets. We further conducted ablation studies to demonstrate the effectiveness of our SLF-HR.

2. Related Work

2.1. Remote HR Estimation

The application of analysing rPPG from camera-captured videos was first proposed by [47]. In early work, many studies have manually designed hand-crafted signal features to characterise the rPPG signals. For example, Poh et al. [39, 38] used independent component analysis (ICA) with RGB colour sequences to estimate HR signals. Similarly, some of methods used chrominance features reflected from the human skin [10, 51, 49]. Although these hand-crafted features have shown promising performance, they require to manually select region of interest (ROI), detect and process skin-pixels signals. This is challenging or even quixotic to be implemented in practical settings. In recent years, deep learning methods based on CNN [46, 18, 32] have been developed to overcome such limitations and they have shown to effectively capture minor colour variation if sufficient training data are available. For example, RhythmNet [34] transformed each video clip into a 2D feature map and fed it into a CNN to estimate HR signals. rPPGNet [56] proposed an end-to-end CNN model to reconstruct rPPG signals from highly-compressed videos. Meta-rPPG [24] applied the concept of meta-learning using 2D CNN coupled with bidirectional long short-term memory (BiLSTM) to learn spatiotemporal features. The performance of these methods, however, were dependent on the availability of labelled data.

2.2. Self-Supervised Video Representations Learning

In recent years, self-supervised representation learning methods has achieved promising results on action recognition task [12, 13, 21]. For instance, Misra et al.[30] learnt video representations by classifying shuffled video clips. Similarly, Jenni et al.[20] experimented a set of temporal transformations and tasked the model to recognise them. The essential concept with these approaches is to use data augmentation to learn invariant features along spatial and temporal space. However, to our best knowledge, none of studies have experimented the effectiveness of standard self-supervised techniques with regard to subtle facial colour changes over the time given that action recognition always involves object interactions with background environment, optical flows, synchronised audios and object tracking. Therefore, we hypothesise that general video representation learning is not optimal for HR estimation.

2.3. Data Augmentation

Spatial augmentations¹ are commonly used in both supervised and self-supervised learning to cover a wider and diverse data distribution, and they have shown to be effective in extracting discriminative image feature space [42, 8, 5, 14, 40, 7]. However, none of previous HR studies [55, 54, 56, 41, 45, 32, 34, 33, 24, 6] have reported to adopt spatial augmentations on frames directly, and the most close one is [35] which horizontally and vertically flip the processed *spatiotemporal map* (a representation to compact the 3D video into 2D).

Motion statistics are essential in representing video information and play a key factor on the success of action recognition [48]. These video dynamics are closely related with temporal information [20]. For instance, [30, 3, 11, 25, 52, 22] proposed to use image frame reordering or optical flows to augment temporal data. However, compared with large-scale body movements, video dynamics like optical flows are not applicable to effectively capture subtle colour variations of each pixel.

3. Method

3.1. HR Representation Learning Framework

The overview of our HR representations learning framework is illustrated in Figure 1. Suppose that we have randomly sampled N raw videos from the dataset. We will then apply our sparsity-based temporal and landmark-based spatial augmentations to generate $2N$ samples in total. Two augmented clips c_i^1, c_i^2 originated from the same video v_i are fed into the 3D ResNet-18 *video encoder* f to obtain features h_i^1, h_i^2 respectively. Both of them are then mapped by the *projection head* g into the space z_i^1, z_i^2 where contrastive loss is applied to maximise mutual information. These two feature vectors are regarded as positive samples and rest of $2(N - 1)$ samples within the same mini-batch are considered as negative samples. We then formulated a contrastive loss function for a positive pair of examples (i, j) according to [5]:

$$\mathcal{L}_{[i,j]} = -\log \frac{\exp(\text{sim}(z_i, z_j)/\tau)}{\sum_{k=0}^{2N} \mathbb{1}_{k \neq i} \exp(\text{sim}(z_i, z_k)/\tau)} \quad (1)$$

where $\mathbb{1}_{k \neq i} \in \{0, 1\}$ is an indicator function which equals to 1 iff $k \neq i$ (i.e., not the feature vector itself) and τ is the temperature hyper-parameter. The loss function gives less penalties if positive samples are more similar to each other than negative samples.

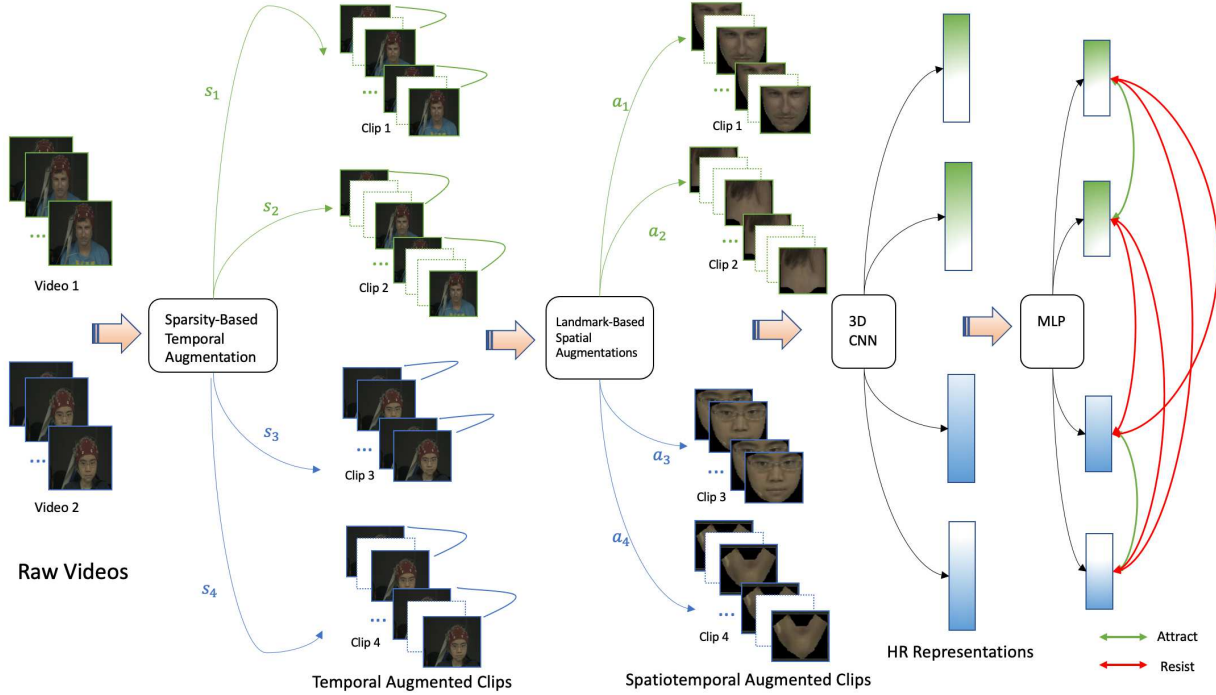


Figure 1. **Overview of our proposed self-supervised framework for HR representations learning.** For a raw RGB video, we first sampled two clips by the sparsity-based temporal augmentation and these two clips had the same number of frames with randomly selected stride. The landmark-based spatial augmentation was then applied to the two clips respectively and fed into a 3D CNN with an multi-layer perceptron (MLP) head projection. Outputs from MLP are evaluated by the contrastive loss function which maximised mutual information.

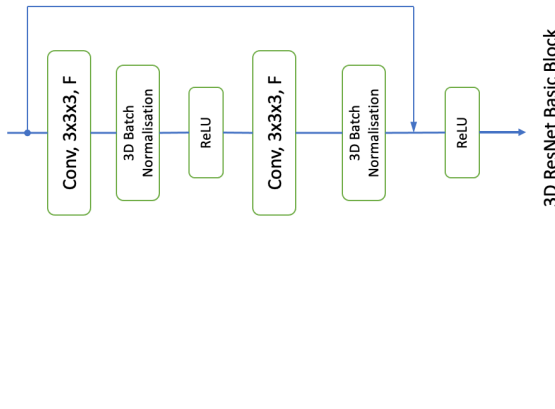


Figure 2. **Basic block for 3D ResNet [15].** F is the number of the layer output features. The arrow refers to the shortcut connection described in 2D ResNet [17].

3.2. Video Encoder and Projection Head

We adopted the ResNet-18 [17] and extended it to a 3D architecture [15] as our backbone which is shown in Table 1.

¹We also consider appearance transformation (such as colour distortion, Gaussian blur) as spatial augmentation, since it mainly focuses on frame-wise information processing.

Layer Name	Layer Structure	Output Size ($C \times D \times H \times W$)
inputs	N/A	$3 \times 30 \times 64^2$
conv ₁	kernel size 7^3 temporal stride 1 spatial stride 2	$64 \times 30 \times 32^2$
max pool	kernel size 3^3 stride 2	$64 \times 15 \times 16^2$
conv ₂	basic block 2	$64 \times 15 \times 16^2$
conv ₃	basic block 2	$128 \times 8 \times 8^2$
conv ₄	basic block 2	$256 \times 4 \times 4^2$
conv ₅	basic block 2	$512 \times 2 \times 2^2$
	global average pool	

Table 1: **Video encoder of SLF-HR: 3D ResNet-18 [15].** Each convolutional layer is followed by a batch normalisation [19] layer and a ReLU layer [31]. The spatiotemporal down-sampling is only applied to conv₃, conv₄ and conv₅ with stride of 2. C denotes the number of channels, D denotes the number of frames, H denotes the height of the frame, and W denotes the width of the frame.

The 3D architecture allows to learn spatial and temporal information at the same time. Each input ($channels \times frames \times height \times width$) was converted into a 512-dimensional feature vector, and then fed into the projection head, which is a multi-layer perceptron (MLP) in our experiment, to obtain the final encoded 512-dimensional feature vector (i.e., z in Equation 1). The last MLP layer is removed during the evaluation process, and the 512-dimensional feature vector from the backbone is used directly as extracted video features to make final HR estimation.

3.3. Skin Reflection Model

According to Shafer's dichromatic reflection model (DRM) [50], assuming light source has a constant spectral composition with varying intensities, the variation of skin reflections over the time are measured based on body motions (specular variations) and pulse-induced subtle colour changes (diffuse reflection) where only diffuse reflection contains HR-related information. Using DRM, we can then define the skin reflection model for the image sequence along the time by

$$C_k(t) = I(t) \cdot (v_s(t) + v_d(t)) + v_n(t) \quad (2)$$

where $C_k(t)$ is the k -th skin pixel of RGB values; $I(t)$ denotes the light intensity level from the light source which is regulated by specular reflection $v_s(t)$ and diffuse reflection $v_d(t)$; $v_n(t)$ is the noise from camera sensor. We can further decompose $v_d(t)$ and $v_s(t)$ by

$$v_s(t) = u_s \cdot (s_0 + s(t)) \quad (3)$$

where u_s is the unit colour vector of the light spectrum, s_0 and $s(t)$ are the stationary and varying parts of specular reflections, i.e., $s(t)$ captures motions.

$$v_d(t) = u_d \cdot d_0 + u_p \cdot p(t) \quad (4)$$

where u_d denotes the unit colour vector of the skin pixel; d_0 refers to the stationary reflection strength; u_p refers to the relative signal strengths in RGB channels; $p(t)$ refers to the HR signal. Given the defined notation above, we can rewrite the Equation 2 using Equation 3, 4 by

$$C_k(t) = I(t) \cdot (u_s \cdot (s_0 + s(t)) + u_d \cdot d_0 + u_p \cdot p(t)) + v_n(t) \quad (5)$$

where our goal is to calculate $p(t)$ from $C_k(t)$.

From Equation 5, our aim is to measure the colour fluctuation defined as u_s and u_d , and to force u_d , determined by the diffuse reflection, dominate the equation and hence maximise HR information we can learn from videos.

3.4. Landmark-based Spatial Augmentation

We defined two criteria for our landmark-based spatial augmentation: 1) the relationship among colour channels

Algorithm 1: Spatiotemporal Augmentation

Input: Video $V = \{v_1, v_2, \dots, v_N\}$ with N frames; Stride list $S = \{s_1, s_2, \dots, s_M\}$ with M values; ROI list $R = \{r_1, r_2, \dots, r_L\}$ with L values; Clip frame number D .

Spatial Augmentation $f_1(v_i)$:

Randomly select a value r_i from R , and generate a clip using ROI r_i only from v_i .

Temporal Augmentation $f_2(v_i)$:

Randomly select a value s_i from S , and generate a D -frame clip with stride of s_i from v_i .

for $k \leftarrow 1, \dots, N$ **do**

// 1st spatiotemporal augmentation

$c_1 = f_1(v_k)$

$c'_1 = f_1(c_1)$

// 2nd spatiotemporal augmentation

$c_2 = f_2(v_k)$

$c'_2 = f_2(c_2)$

end

Output: Augmented video clips

$$V' = \{c'_1, c'_2, \dots, c'_{2N-1}, c'_{2N}\}$$

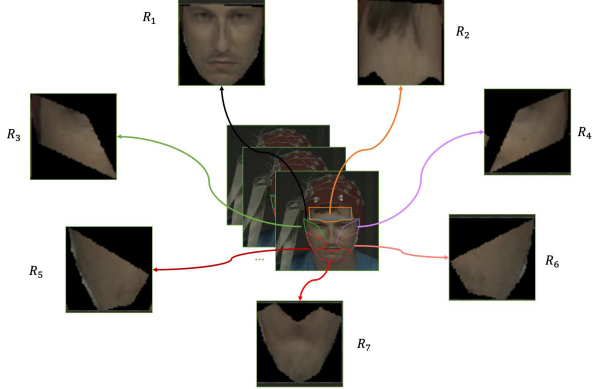


Figure 3. **Illustration of landmark-based spatial augmentation.** Based on detected facial landmarks, we define 7 ROI areas: the whole face, forehead, left top cheek, right top cheek, left bottom cheek, right bottom cheek and chin corresponding to $\{R_1, R_2, R_3, R_4, R_5, R_6, R_7\}$ respectively. Every call of spatial augmentation will randomly select one ROI and crop it over the whole clip.

of each pixel needs to be considered; and 2) various diffusion reflections from selected ROIs need to be considered. As such, we cropped each frame into several facial parts according to face landmark locations [4] as shown in Fig 3. The selection of ROIs considers two factors: 1) The movements of eyes and mouth are more rapid than other facial parts which generate noisy data; and 2) facial parts

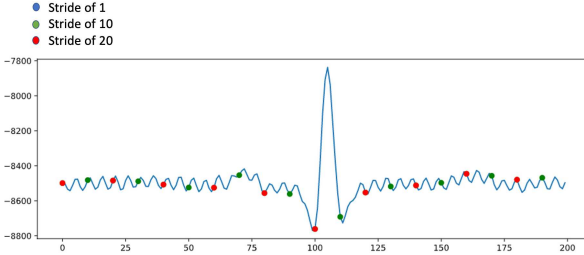


Figure 4. **Illustration of signal sparsity.** The given signal example comes from MAHNOB-HCI dataset [44] with sampling rate of 256 and this is the shape of 1 second signal. The blue line represents original signal shape (i.e., stride of 1), the green dots represent data points of stride of 10, and the red dots represent data points of stride of 20. **Note:** red points overlap with green points i.e. green points also appear at red point positions.

with similar colour should contain similar signals. Theoretically, removal of non-facial areas filters noise from the background which reduces the weight of $v_n(t)$ in Equation 5. Informative ROIs ensure the dominance of diffusion reflections u_d and different ROI sequences from the same facial video are supposed to contain similar HR signals despite of different weights of u_s and u_d . In this paper, we define 7 ROIs including the whole face, forehead, left top cheek, right top cheek, left bottom cheek, right bottom cheek and chin. During the training phase, they are randomly selected along the same video clip.

3.5. Sparsity-based Temporal Augmentation

The main idea of sparsity-based temporal augmentation is motivated by the physical property of signals as shown in 4, i.e., Nyquist–Shannon sampling theorem [36] such that a discrete sequence of samples can reconstruct corresponding continuous-time signal if the band-limit B of the signal is less than the sample rate f_s , i.e., $B < \frac{1}{2}f_s$. In our case, the Frames Per Second (FPS) can be treated as sampling rate, and as long as the FPS is bigger than the Nyquist rate (i.e., 2 times of HR signal band-limit), the video clip can represent all information contained in the HR signal. Therefore, we can augment each video along the time-axis by applying random strides given that clips with smaller FPS contain more sparse signals when sampling from a same-length video. To compensate the loss of information in terms of the sparsity, the large-sparsity video clip will have more information in terms of the length (i.e., the clip is generated by a longer video).

4. Experiment

We evaluated our HR estimation framework on three widely used public datasets: MAHNOB-HCI [44], VIPL-HR-V2 [28] and UBFC-rPPG [2]. Final model performance

is measured by comparing the average HR values estimation errors with metrics of standard deviation (SD), the mean absolute error (MAE), the root mean square error (RMSE) and the Pearson’s correlation coefficient (R). During the evaluation process, we adopt subject-exclusive test [34], i.e., subjects in the training set will not appear in the testing set for fair comparisons.

4.1. Datasets

MAHNOB-HCI [44] contains 27 subjects, including 12 males and 15 females, who participated in two experiments: *a. emotion elicitation*; *b. implicit tagging*. Each video was recorded in 780×580 resolution with FPS of 61. Following the previous settings [27], we used RGB videos recorded in *emotion elicitation experiment* and selected part of frames in the range from 306 to 2135 (around 30 seconds), which resulted in 527 videos. To make fair comparisons with other two datasets, we also down-sampled each video into 30 FPS by removing half of video frames per second. The ground truth HRs were calculated from ECG signals in the channel *EXG2*.

VIPL-HR-V2 [28] is a recently released large-scale HR estimation benchmark which contains 2,500 RGB videos of 500 subjects recorded in 960×720 resolution with FPS of 30 in average. This dataset is recognised to be more challenging as it introduces more realistic scenarios including various head movements, illumination variations and wide range of HR values [33]. Ground truth HRs and FPS are provided for each video.

UBFC-rPPG [2] contains 42 uncompressed videos from 42 subjects. Ground truth HRs, measured per second, are provided for the videos. In our experiments, we augmented each video by using a sliding window of 150 frames without any frame overlap, i.e., 60 seconds video was split into 12 clips of 5 seconds each. We obtained 523 videos after the augmentation.

All videos were resized into the size of 64×64 . The training and testing datasets split used the ratio of 8 : 2.

4.2. Evaluation

To evaluate the extracted HR representations, we followed the common linear classification protocol [5, 16] which froze all of backbone layers and trained a linear classifier i.e., a fully-connected (FC) layer to make the final HR predictions. Firstly, we evaluated our SLF-HR performance by comparing with previous state-of-art self-supervised video representation learning work including DPC [12], MemDPC [13] and SeCo [53] which were trained on MAHNOB-HCI training set without labels and validated on the MAHNOB-HCI testing dataset. Moreover, we also compared our method with other supervised approaches including baseline 3D ResNet-18 and previous state-of-art supervised HR estimation methods on

Strategy	Method	Network	Dataset	HR (bpm)			
				SD	MAE	RMSE	R
Self-Supervised	DPC [12]	3D ResNet-18	MAHNOB-HCI	-	9.16	-	-
	MemDPC [13]	(2+3D)-ResNet18	MAHNOB-HCI	-	8.23	-	-
	SeCo [53]	ResNet18	MAHNOB-HCI	-	7.03	-	-
Supervised	SLF-HR	3D ResNet-18	MAHNOB-HCI	5.35	4.25	5.36	0.89
		3D ResNet-18	VIPL-HR-V2	18.05	13.69	18.04	0.16
Supervised	Supervised Baseline	3D ResNet-18	MAHNOB-HCI	9.81	7.34	9.76	0.56
	DeepPhys [6]	N/A		-	4.57	-	-
	STVEN + rPPGNet [56]	N/A		5.57	4.03	5.93	0.88
	Meta-rPPG (Proto+synth) [24]	N/A	VIPL-HR-V2	4.90	3.01	3.68	0.85
	Supervised Baseline	3D ResNet-18		16.69	12.03	16.68	0.37
Supervised	RePSS Team 1 [28]	N/A	VIPL-HR-V2	-	8.50	-	-
	RePSS Team 1 [28]	N/A		-	12.00	-	-

Table 2: **Linear evaluation results.** We evaluated our model on MAHNOB-HCI and VIPL-HR-V2 datasets comparing with supervised baseline and previous state-of-art methods.

MAHNOB-HCI and VIPL-HR-V2.

As for the transfer learning, we designed three paradigms: a. self-supervised pre-training strategy; b. pre-train on large dataset and fine-tune on small dataset; c. pre-train on small dataset and fine-tune on large dataset. We firstly trained SLF-HR on the training set (MAHNOB-HCI, VIPL-HR-V2) without labels, and then fine-tuned the whole model in the testing set (MAHNOB-HCI, VIPL-HR-V2, UBFC-rPPG) with labels. We also compared our method with 3D ResNet-18 pre-trained on Kinetics-700 [43] dataset as well as the fine-tuned 3D ResNet-18 using MAHNOB-HCI.

4.3. Implementation Details

Self-Supervised Training. Each video was first augmented into two clips using the stride number randomly sampled from the list $\{1, 2, 3, 4, 5\}$, and each clip was constrained to have length of 30-frame. Therefore, the longest clip (i.e., stride of 5) contained 5-second information, while the shortest clip (i.e., stride of 1) had only 1-second information. Frames of each clip were then cropped to a specific ROI by randomly selecting from 7 predefined facial areas as described in Section 3.4. For MAHNOB-HCI dataset, the hyper-parameter τ in Equation 1 was 0.1, output dimension of MLP with 512, learning rate of 1e-5, batch size of 128, and epoch number with 200. For VIPL-HR-V2 dataset, the hyper-parameter τ was 0.5, output dimension of MLP with 2048, learning rate of 1e-6, batch size of 128, and epoch number with 500. We used Adam [23] optimiser with default settings to update the model weights.

Linear Classification Evaluation. We aligned the training process with self-supervised settings by sampling 75-frame clips with the stride of 2 from 150-frame videos. The learning rate was set to 5e-3 and the epoch number was set to 50.

5. Results and Discussions

5.1. Linear Classification Evaluation

Experiment results using linear classification evaluation are shown in Table 3. Our method had better accuracy than other self-supervised video representation learning methods on MAHNOB-HCI, achieving the MAE of 4.25 and we attribute this to our robust landmark-based spatial and sparsity-based temporal augmentation schemes that effectively captured subtle colour fluctuations on facial skin. SeCo [53] was the closest to our method achieving MAE of 7.03. It, however, used 2D CNN architecture and did not fully exploit the whole 3D information. The baseline supervised 3D ResNet-18 had lower accuracy than our method and this is mainly due to the limited labelled data size of MAHNOB-HCI that made model became overfitting. Our method also had competitive accuracy with state-of-the-art DeepPhys [6] (MAE of 4.57) and rPPGNet [56] (MAE of 4.03). The best performing approach was the Meta-rPPG [24] (MAE of 3.01).

The VIPL-HR-V2 dataset contains more complex video conditions and so, in comparison to the MAHNOB-HCI, the overall performance of all the methods was reduced. Nevertheless, our method still performed well with a MAE of 13.69 and had competitive accuracy with baseline supervised 3D ResNet-18 (MAE of 12.03) and RePSS Team 1 (MAE of 8.5).

5.2. Transfer Learning

The results of the transfer learning are shown in Table 3. Our results show that our SLF-HR was able to improve the estimation of HR when it was used to pre-train CNNs for subsequent supervised fine-tuning. It improved the performance of supervised baseline 3D-ResNet-18 from MAE

Method	Paradigm	Pre-training Dataset	Fine-tuned Dataset	HR (bpm)			
				SD	MAE	RMSE	R
SLF-HR	a	MAHNOB-HCI	MAHNOB-HCI	9.09	6.79	9.68	0.84
	b	VIPL-HR-V2	MAHNOB-HCI	10.19	6.23	10.35	0.56
	b	VIPL-HR-V2	UBFC-rPPG	11.06	7.83	11.14	0.57
	c	MAHNOB-HCI	VIPL-HR-V2	15.58	11.52	15.62	0.47
3D ResNet-18 [15]	N/A	Kinetics-700	MAHNOB-HCI	11.89	8.98	13.03	-0.07

Table 3: **Transfer learning results.** We designed three paradigms: a. self-supervised pre-training strategy; b. pre-train on large dataset and fine-tune on small dataset; c. pre-train on small dataset and fine-tune on large dataset.

of 7.34 to 6.79 on MAHNOB-HCI dataset. It also generated greater performance when the larger VIPL-HR-V2 dataset was used for pre-training (MAE of 6.23). Similarly, our method also reduced the MAE score of supervised baseline method from 8.33 to 7.83 on UBFC-rPPG dataset. We suggest that our self-supervised pre-training acted as an initialisation point for effective supervised fine-tuning, which improved the feature representation of HR signals. Our method also had a greater accuracy than the supervised 3D ResNet-18 which was pre-trained using Kinetics-700 labelled data (MAE of 8.98) on MAHNOB-HCI dataset.

5.3. Ablation Study

Landmark-based Spatial Augmentation

We compared our landmark-based spatial augmentation with 5 other common data augmentation techniques including *Random Crop and Resize*, *Random Horizontal Flip*, *Colour Jitter*, *Random Grayscale* and *Gaussian Blur*. We applied these techniques to the face area (i.e., R_1 of the pre-defined ROI list) and used stride of 1 to avoid temporal augmentation effects. We used the same settings in the linear classification evaluation and MAHNOB-HCI dataset for comparative analysis. As shown in Table 4, our landmark-based spatial augmentation had the best MAE score of 5.12. Furthermore, our results show that adding global face information (R_1) can guide the model to better understand HR features which improved MAE of 7.98 to 5.12. Besides, we also combined our landmark-based spatial augmentation scheme with other standard spatial augmentation techniques. The best result (MAE of 5.24) was yielded by combining *Random Horizontal Flip* and our landmark-based augmentation. Among the standard augmentation techniques, *Random Crop and Resize* had the best result with MAE of 6.74. *Random Grayscale* had the worst performance with MAE of 10.66. The combination of all 5 techniques, in fact, reduced the performance with MAE of 9.54. One possible reason is that *although appearance transformations prevent the model from using colour histogram shortcut [5] to distinguish different views, HR-related information contained in colour channels are also distorted*. Another reason is that *geometric transformations cannot*

Method	HR (bpm) MAE
Random Crop and Resize	6.74
Random Horizontal Flip	6.99
Colour Jitter	8.11
Random Grayscale	10.66
Gaussian Blur	9.81
Combined Above 5 Augmentations	9.54
ROIs (not include face)	7.98
ROIs (include face)	5.12
ROIs (include face) + Random Crop and Resize	7.34
ROIs (include face) + Random Horizontal Flip	5.24
ROIs (include face) + Colour Jitter	8.19
ROIs (include face) + Random Grayscale	8.13
ROIs (include face) + Gaussian Blur	7.02

Table 4: **Ablation study on spatial augmentation.** We evaluated 5 commonly used spatial augmentations and their combinations. Our landmark-based spatial augmentation outperforms other methods.

guarantee augmented inputs are valuable, since they may introduce signal noise by including non-facial areas [27]. Overall, our landmark-based spatial augmentation outperformed standard spatial augmentation techniques by a large margin for the task of HR estimation.

Sparsity-based Temporal Augmentation

We evaluated the effectiveness of our sparsity-based temporal augmentation compared to different temporal augmentation techniques including *Random Temporal Interval* [40], *Random Permutation* [20], *Periodic* [20] and *Warp* [20]. We used the same settings in the linear classification evaluation and MAHNOB-HCI dataset for comparative analysis. As shown in Table 5, our sparsity-based temporal augmentation outperformed other augmentation techniques with MAE of 5.28. Among these four standard temporal augmentations, *Random Temporal Interval* had the best result with MAE of 5.74 and we attribute this to its ability of characterising the periodic cycle of blood volume changes on facial skin. *Periodic* had the worst MAE score of 7.31 and this is because it distorted the HR signals. We also investigated the possible value range of the strides in Figure 5 and our results show that the MAE scores was bet-

Method	HR (bpm) MAE
Random Temporal Interval [40]	5.74
Random Permutation [20]	7.18
Periodic [20]	7.31
Warp [20]	7.22
Sparsity-based from $\{1, 2, 3, 4, 5\}$	5.28

Table 5: Ablation study on temporal augmentation. We evaluated 4 temporal augmentations proposed in previous studies. Our sparsity-based temporal augmentation outperformed others and the *Random Temporal Interval* yield best results among 4 common temporal augmentations.

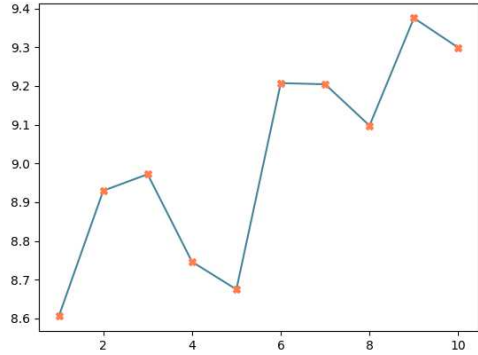


Figure 5. Ablation study on temporal stride range. We evaluate possible value range of stride and find a positive relationship between stride number and MAE.

Model Architecture	HR (bpm)			
	SD	MAE	RMSE	R
3D ResNet-18	5.35	4.25	5.36	0.89
3D ResNet-34	5.37	4.34	5.64	0.89
3D ResNet-50	11.39	5.46	11.38	0.39

Table 6: Ablation studies on backbone architecture. We evaluated different model architecture on MAHNOB-HCI.

ter with smaller stride size.

Different CNN Architectures

We also evaluated our method with different CNN architectures using MAHNOB-HCI dataset. Our results show that smaller CNN models such as 3D ResNet-18 coupled with our SLF-HR had better performance (MAE of 4.25) than other larger CNN models (MAE of 5.46) as shown in Table 6.

6. Conclusion

In this paper, we presented a new self-supervised learning framework for remote HR estimation using spatiotemporal augmentation. A novel landmark-based spatial augmentation and a sparsity-based temporal augmentation are proposed to effectively capture subtle colour changes on facial skin. We evaluated our framework using three public datasets and compared with other state-of-the-art self-supervised and supervised learning methods. Our results show that our framework outperformed other self-supervised learning methods and achieved a competitive accuracy compared to other supervised methods. Our findings indicate that our framework can be used to learn discriminative image features when there are none or limited labelled data.

References

- [1] Euijoon Ahn, Ashnil Kumar, M. Fulham, D. Feng, and Jinman Kim. Unsupervised domain adaptation to classify medical images using zero-bias convolutional auto-encoders and context-based feature augmentation. *IEEE Transactions on Medical Imaging*, 39:2385–2394, 2020.
- [2] S. Bobbia, R. Macwan, Y. Benezeth, A. Mansouri, and Julien Dubois. Unsupervised skin tissue segmentation for remote photoplethysmography. *Pattern Recognit. Lett.*, 124:82–90, 2019.
- [3] B. Brattoli, U. Büchler, A. Wahl, M. Schwab, and B. Ommer. Lstm self-supervision for detailed behavior analysis. *2017 IEEE Conference on Computer Vision and Pattern Recognition (CVPR)*, pages 3747–3756, 2017.
- [4] Adrian Bulat and Georgios Tzimiropoulos. How far are we from solving the 2d & 3d face alignment problem? (and a dataset of 230,000 3d facial landmarks). *2017 IEEE International Conference on Computer Vision (ICCV)*, pages 1021–1030, 2017.
- [5] Ting Chen, Simon Kornblith, Mohammad Norouzi, and Geoffrey E. Hinton. A simple framework for contrastive learning of visual representations. *ArXiv*, abs/2002.05709, 2020.
- [6] W. Chen and D. McDuff. Deepphys: Video-based physiological measurement using convolutional attention networks. *ArXiv*, abs/1805.07888, 2018.
- [7] Xinlei Chen, Haoqi Fan, Ross B. Girshick, and Kaiming He. Improved baselines with momentum contrastive learning. *ArXiv*, abs/2003.04297, 2020.
- [8] E. D. Cubuk, Barret Zoph, Jonathon Shlens, and Quoc V. Le. Randaugment: Practical automated data augmentation with a reduced search space. *2020 IEEE/CVF Conference on Computer Vision and Pattern Recognition Workshops (CVPRW)*, pages 3008–3017, 2020.
- [9] G. de Haan and V. Jeanne. Robust pulse rate from chrominance-based rppg. *IEEE Transactions on Biomedical Engineering*, 60(10):2878–2886, Oct 2013.
- [10] Gerard De Haan and Vincent Jeanne. Robust pulse rate from chrominance-based rppg. *IEEE Transactions on Biomedical Engineering*, 60(10):2878–2886, 2013.

[11] Basura Fernando, Hakan Bilen, E. Gavves, and Stephen Gould. Self-supervised video representation learning with odd-one-out networks. *2017 IEEE Conference on Computer Vision and Pattern Recognition (CVPR)*, pages 5729–5738, 2017.

[12] Tengda Han, Weidi Xie, and Andrew Zisserman. Video representation learning by dense predictive coding. *2019 IEEE/CVF International Conference on Computer Vision Workshop (ICCVW)*, pages 1483–1492, 2019.

[13] Tengda Han, Weidi Xie, and Andrew Zisserman. Memory-augmented dense predictive coding for video representation learning. In *ECCV*, 2020.

[14] Tengda Han, Weidi Xie, and Andrew Zisserman. Self-supervised co-training for video representation learning. *ArXiv*, abs/2010.09709, 2020.

[15] Kensho Hara, Hirokatsu Kataoka, and Yutaka Satoh. Can spatiotemporal 3d cnns retrace the history of 2d cnns and imagenet? In *Proceedings of the IEEE Conference on Computer Vision and Pattern Recognition (CVPR)*, pages 6546–6555, 2018.

[16] Kaiming He, Haoqi Fan, Yuxin Wu, Saining Xie, and Ross B. Girshick. Momentum contrast for unsupervised visual representation learning. *2020 IEEE/CVF Conference on Computer Vision and Pattern Recognition (CVPR)*, pages 9726–9735, 2020.

[17] Kaiming He, X. Zhang, Shaoqing Ren, and Jian Sun. Deep residual learning for image recognition. *2016 IEEE Conference on Computer Vision and Pattern Recognition (CVPR)*, pages 770–778, 2016.

[18] Gee-Sern Hsu, ArulMurugan Ambikapathi, and Ming-Shiang Chen. Deep learning with time-frequency representation for pulse estimation from facial videos. In *2017 IEEE International Joint Conference on Biometrics (IJCB)*, pages 383–389. IEEE, 2017.

[19] S. Ioffe and Christian Szegedy. Batch normalization: Accelerating deep network training by reducing internal covariate shift. *ArXiv*, abs/1502.03167, 2015.

[20] S. Jenni, Givi Meishvili, and P. Favaro. Video representation learning by recognizing temporal transformations. *ArXiv*, abs/2007.10730, 2020.

[21] Longlong Jing and Yingli Tian. Self-supervised spatiotemporal feature learning by video geometric transformations. *ArXiv*, abs/1811.11387, 2018.

[22] Dahun Kim, Donghyeon Cho, and In-So Kweon. Self-supervised video representation learning with space-time cubic puzzles. In *AAAI*, 2019.

[23] Diederik P. Kingma and Jimmy Ba. Adam: A method for stochastic optimization. *CorR*, abs/1412.6980, 2015.

[24] Eugene Lee, E. Chen, and C. Lee. Meta-rppg: Remote heart rate estimation using a transductive meta-learner. In *ECCV*, 2020.

[25] Hsin-Ying Lee, Jia-Bin Huang, Maneesh Kumar Singh, and Ming-Hsuan Yang. Unsupervised representation learning by sorting sequences. *2017 IEEE International Conference on Computer Vision (ICCV)*, pages 667–676, 2017.

[26] Xiaobai Li, I. Alikhani, J. Shi, T. Seppänen, J. Junttila, Kirsi Majamaa-Voltti, M. Tulppo, and G. Zhao. The obf database: A large face video database for remote physiological signal measurement and atrial fibrillation detection. *2018 13th IEEE International Conference on Automatic Face & Gesture Recognition (FG 2018)*, pages 242–249, 2018.

[27] Xiaobai Li, J. Chen, G. Zhao, and M. Pietikäinen. Remote heart rate measurement from face videos under realistic situations. *2014 IEEE Conference on Computer Vision and Pattern Recognition*, pages 4264–4271, 2014.

[28] Xiao-Bai Li, Hu Han, H. Lu, Xue-Song Niu, Z. Yu, A. Dantcheva, G. Zhao, and S. Shan. The 1st challenge on remote physiological signal sensing (repss). *2020 IEEE/CVF Conference on Computer Vision and Pattern Recognition Workshops (CVPRW)*, pages 1274–1281, 2020.

[29] D. J. McDuff, J. R. Estepp, A. M. Piasecki, and E. B. Blackford. A survey of remote optical photoplethysmographic imaging methods. In *2015 37th Annual International Conference of the IEEE Engineering in Medicine and Biology Society (EMBC)*, pages 6398–6404, Aug 2015.

[30] I. Misra, C. L. Zitnick, and M. Hebert. Shuffle and learn: Unsupervised learning using temporal order verification. In *ECCV*, 2016.

[31] V. Nair and Geoffrey E. Hinton. Rectified linear units improve restricted boltzmann machines. In *ICML*, 2010.

[32] Xuesong Niu, Hu Han, S. Shan, and X. Chen. Synrhythm: Learning a deep heart rate estimator from general to specific. *2018 24th International Conference on Pattern Recognition (ICPR)*, pages 3580–3585, 2018.

[33] Xuesong Niu, Hu Han, S. Shan, and X. Chen. Viplhr: A multi-modal database for pulse estimation from less-constrained face video. In *ACCV*, 2018.

[34] Xuesong Niu, S. Shan, Hu Han, and X. Chen. Rhythmnnet: End-to-end heart rate estimation from face via spatial-temporal representation. *IEEE Transactions on Image Processing*, 29:2409–2423, 2020.

[35] Xuesong Niu, Z. Yu, Hu Han, Xiaobai Li, S. Shan, and G. Zhao. Video-based remote physiological measurement via cross-verified feature disentangling. In *ECCV*, 2020.

[36] H. Nyquist. Certain topics in telegraph transmission theory. *Transactions of the American Institute of Electrical Engineers*, 47:617–644.

[37] A. Oord, Y. Li, and Oriol Vinyals. Representation learning with contrastive predictive coding. *ArXiv*, abs/1807.03748, 2018.

[38] Ming-Zher Poh, Daniel J McDuff, and Rosalind W Picard. Advancements in noncontact, multiparameter physiological measurements using a webcam. *IEEE transactions on biomedical engineering*, 58(1):7–11, 2010.

[39] Ming-Zher Poh, Daniel J McDuff, and Rosalind W Picard. Non-contact, automated cardiac pulse measurements using video imaging and blind source separation. *Optics express*, 18(10):10762–10774, 2010.

[40] Rui Qian, Tianjian Meng, Boqing Gong, Ming-Hsuan Yang, H. Wang, Serge J. Belongie, and Yin Cui. Spatiotemporal contrastive video representation learning. *arXiv: Computer Vision and Pattern Recognition*, 2020.

[41] Y. Qiu, Y. Liu, J. Arteaga-Falconi, H. Dong, and A. E. Saddik. Evm-cnn: Real-time contactless heart rate estima-

tion from facial video. *IEEE Transactions on Multimedia*, 21:1778–1787, 2019.

[42] Connor Shorten and T. Khoshgoftaar. A survey on image data augmentation for deep learning. *Journal of Big Data*, 6:1–48, 2019.

[43] Lucas Smaira, J. Carreira, Eric Noland, Ellen Clancy, A. Wu, and Andrew Zisserman. A short note on the kinetics-700-2020 human action dataset. *ArXiv*, abs/2010.10864, 2020.

[44] M. Soleymani, J. Lichtenauer, T. Pun, and M. Pantic. A multimodal database for affect recognition and implicit tagging. *IEEE Transactions on Affective Computing*, 3:42–55, 2012.

[45] Radim Spetlik, Vojtech Franc, J. Cech, and Jiri Matas. Visual heart rate estimation with convolutional neural network. In *BMVC*, 2018.

[46] Sergey Tulyakov, Xavier Alameda-Pineda, Elisa Ricci, Lijun Yin, Jeffrey F Cohn, and Nicu Sebe. Self-adaptive matrix completion for heart rate estimation from face videos under realistic conditions. In *Proceedings of the IEEE Conference on Computer Vision and Pattern Recognition*, pages 2396–2404, 2016.

[47] Wim Verkruyse, Lars O Svaasand, and J Stuart Nelson. Remote plethysmographic imaging using ambient light. *Optics express*, 16(26):21434–21445, 2008.

[48] Jiangliu Wang, Jianbo Jiao, Linchao Bao, Shengfeng He, Yunhui Liu, and W. Liu. Self-supervised spatio-temporal representation learning for videos by predicting motion and appearance statistics. *2019 IEEE/CVF Conference on Computer Vision and Pattern Recognition (CVPR)*, pages 4001–4010, 2019.

[49] Wenjin Wang, Albertus C den Brinker, Sander Stuijk, and Gerard de Haan. Algorithmic principles of remote ppg. *IEEE Transactions on Biomedical Engineering*, 64(7):1479–1491, 2016.

[50] W. Wang, Albertus C. den Brinker, S. Stuijk, and G. de Haan. Algorithmic principles of remote ppg. *IEEE Transactions on Biomedical Engineering*, 64:1479–1491, 2017.

[51] Wenjin Wang, Sander Stuijk, and Gerard De Haan. Exploiting spatial redundancy of image sensor for motion robust rppg. *IEEE transactions on Biomedical Engineering*, 62(2):415–425, 2014.

[52] D. Xu, Jun Xiao, Zhou Zhao, J. Shao, Di Xie, and Y. Zhuang. Self-supervised spatiotemporal learning via video clip order prediction. *2019 IEEE/CVF Conference on Computer Vision and Pattern Recognition (CVPR)*, pages 10326–10335, 2019.

[53] Ting Yao, Yiheng Zhang, Zhaofan Qiu, Yingwei Pan, and Tao Mei. Seco: Exploring sequence supervision for unsupervised representation learning. *ArXiv*, abs/2008.00975, 2020.

[54] Z. Yu, Xiaobai Li, Xuesong Niu, J. Shi, and G. Zhao. Autohr: A strong end-to-end baseline for remote heart rate measurement with neural searching. *IEEE Signal Processing Letters*, 27:1245–1249, 2020.

[55] Z. Yu, Xiao-Bai Li, and G. Zhao. Remote photoplethysmograph signal measurement from facial videos using spatio-temporal networks. In *BMVC*, 2019.

[56] Z. Yu, Wei Peng, Xiao-Bai Li, Xiaopeng Hong, and G. Zhao. Remote heart rate measurement from highly compressed facial videos: An end-to-end deep learning solution with video enhancement. *2019 IEEE/CVF International Conference on Computer Vision (ICCV)*, pages 151–160, 2019.